Journal of Materials Chemistry C

Accepted Manuscript

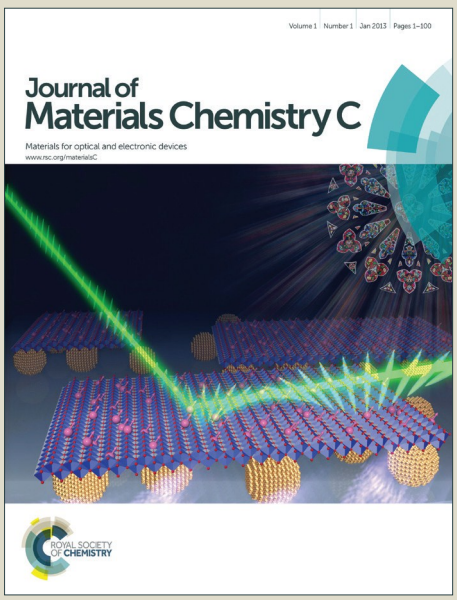

ROYAL SOCIETY OF CHEMISTRY

www.rsc.org/materialsC

$RE_3Sb_3Zn_2O_{14}$ (RE=La, Pr, Nd, Sm, Eu, Gd): A new family of pyrochlore derivatives with rare earth ions on a 2D Kagome lattice

M.B. Sanders, J.W. Krizan, and R.J. Cava

Department of Chemistry, Princeton University, Princeton, New Jersey 08544

Abstract

We report the synthesis and crystal structures of compounds of the type $RE_3Sb_3Zn_2O_{14}$ ($La_3Sb_3Zn_2O_{14}$, $Pr_3Sb_3Zn_2O_{14}$, $Nd_3Sb_3Zn_2O_{14}$, $Sm_3Sb_3Zn_2O_{14}$, $Eu_3Sb_3Zn_2O_{14}$, and $Gd_3Sb_3Zn_2O_{14}$), a series of novel rhombohedral pyrochlore derivatives with rare earth ions on a two-dimensional Kagome lattice. Synchrotron powder x-ray diffraction was used to solve the structures of the compounds. The rare earth ions are fully atomically ordered in a symmetric magnetic Kagome lattice. The nonmagnetic lattice contains one ion (Zn) that is displaced from the center of its coordination polyhedron in a random fashion. The structure differs from the common cubic $A_2B_2O_7$ pyrochlore type because it forms a layered rather than three-dimensional structure through ordering of $ZnRE_3$ in the A sites and $ZnSb_3$ in the B sites. Magnetic property measurements indicate the compounds display dominantly antiferromagnetic interactions between spins, and no signs of magnetic ordering above 1.8 K except possibly the Pr and Eu cases. $RE_3Sb_3Zn_2O_{14}$ is the first series of this structure type in which the rare earth is the only magnetic ion in the structure. This family is therefore an archetype for exploring rare earth magnetism on a two-dimensional Kagome lattice.

Introduction

Compounds with the $A_2B_2O_7$ pyrochlore structure are of great interest due to their varied physical properties, comprising materials like electronic insulators ($La_2Zr_2O_7$), ionic conductors ($Gd_2Zr_2O_7$), metallic conductors ($Bi_2Ru_2O_7$), spin ices ($Dy_2Ti_2O_7$), spin glasses ($Y_2Mo_2O_7$), and superconductors ($Cd_2Re_2O_7$).[1,2,3,4,5,6] The pyrochlore structure crystallizes in the cubic space group *Fd-3m*, where the A and B cations form two interpenetrating networks of tetrahedra. When either the A or B sites is magnetic, the system may experience geometric magnetic frustration, a phenomenon where competing magnetic interactions cannot be simultaneously satisfied. Pyrochlores with magnetic rare earth ions on the A site have been of particular interest.[7]

The three-dimensional (3D) pyrochlore structure may also be viewed in a layered manner, in which A_3B and B_3A layers are A-based and B-based Kagome planes with B cations and A ions residing in the non-Kagome positions, respectively. Similar to the 3D pyrochlore lattice, the 2D Kagome lattice is recognized as one of the most geometrically frustrating magnetic systems.[8] As a means of investigating magnetic frustration on the Kagome lattice, several studies have been performed to isolate the 2D Kagome planes within the 3D pyrochlore structure by placing nonmagnetic atoms in an appropriate, ordered way in the pyrochlore network. Examples of such experiments on pyrochlore-related structures include Th and Al-doped zirconolite ($CaZrTi_2O_7$) and Nd and Zr-doped weberite ($Ca_2Ta_2O_7$), each of which possesses Kagome layers.[9] However, they also contain significant amounts of compositional or structural defects, which, due to the resulting strong structural disorder, hinder the ability to characterize the magnetism of their Kagome lattices.

For the purpose of comparing magnetic frustration in two and three dimensions, the 3D pyrochlore is frequently juxtaposed with structures containing 2D Kagome lattices. For transition metals, the "Herbertsmithite" compound often serves this purpose, with its Kagome planes composed of copper ions.[10,11,12,13] 2D Kagome planes of rare earth ions, however, are very rare. Aside from the langasites, such as $Pr_3Ga_5SiO_{14}$ and $Nd_3Ga_5SiO_{14}$, which are based on "breathing" Kagome planes (i.e. consisting of alternating larger and smaller rare earth triangles), there are currently no known rare earth-based materials with ideal Kagome lattices that can be compared to the frequently-studied rare earth pyrochlores.[14,15]

Here we report the crystal structures and elementary magnetic properties of compounds in the $RE_3Sb_3Zn_2O_{14}$ family (RE=La, Pr, Nd, Sm, Eu, Gd), a series of new materials with a crystallographically ordered, ideal rare earth 2D Kagome lattice. The new series reported here, $RE_3Sb_3Zn_2O_{14}$, is similar to the $RE_3Sb_3Mn_2O_{14}$ (RE=La, Pr, and Nd) and $RE_3Sb_3Co_2O_{14}$ (RE=La, Pr, Nd, Sm-Ho), both based on magnetic transition elements, which have recently been reported to crystallize in a rhombohedral space group closely related to the pyrochlore.[16,17] This structure type, adopted by the new $RE_3Sb_3Zn_2O_{14}$ materials, is fully layered, with the rare earth ions in an ordered, symmetric Kagome array. The structure is similar to the cubic $A_2B_2O_7$ pyrochlore structure, but has rare earth ions on an ideal Kagome lattice with Zn:RE in the A sites and Zn:Sb in the B sites in the ratio 1:3 (Figure 1). This is in strict contrast to the common pyrochlore, which has magnetic ions connecting its Kagome planes. The distinct Kagome lattices constructed by RE^{3+} and Sb^{5+} that compose $[RE_3Zn][Sb_3Zn]O_{14}$ make the structure a model for investigating magnetic frustration in an idealized 2-dimensional pyrochlore-based Kagome system.

Experimental

Powder samples of $RE_3Sb_3Zn_2O_{14}$ were synthesized by solid-state reaction. The starting materials used for the synthesis were La_2O_3, Pr_6O_{11}, Nd_2O_3, Sm_2O_3, Eu_2O_3, Gd_2O_3, ZnO, and Sb_2O_3. The rare earth oxides were first dried overnight at 800 °C. Stoichiometric amounts of reagents were intimately mixed in an agate mortar and pestle and pre-reacted in air in alumina crucibles at 1000 °C for 15 hours. Samples were then reground and heated at 1200 °C for 60 hours in air with intermediate regrinding and reheating. Attempts to synthesize materials with the same structure based on smaller rare earth ions were unsuccessful.

The X-ray powder diffraction data for the crystal structure determinations of $RE_3Sb_3Zn_2O_{14}$ were collected at room temperature using beamline 11-BM at the Advanced Photon Source (APS) at Argonne National Laboratory (λ=0.414 Å). Structural refinements employing the synchrotron x-ray data were carried out by the Rietveld method using the program Fullprof. The magnetic susceptibilities of $RE_3Sb_3Zn_2O_{14}$ were measured between 1.8 and 300 K in a Quantum Design Physical Properties Measurement System (PPMS) in an applied field of 5000 Oe. The magnetizations were linearly proportional to magnetic field for all temperatures

above 1.8 K to fields of approximately 15,000 Oe in all materials, and thus the magnetic susceptibility was defined as M/H at an intermediate field of H=5000 Oe.

Results and discussion

Crystal Structure of $RE_3Sb_3Zn_2O_{14}$

The structures were refined in the space group *R-3m*, initially with the Zn ions on sites 3a and 3b and the RE and Sb ions are on sites 9e and 9d, respectively. The oxygens were initially placed in the positions found in $La_3Sb_3Mn_2O_{14}$ as a model.[16] Rietveld refinements proceeded smoothly to obtain the final models; all the $RE_3Sb_3Zn_2O14$ compounds studied here are isostructural. The results of the refinements are summarized in Table 1. Figures 2 through 4 compare the observed powder x-ray diffraction patterns to those calculated for the final structural models. The high quality of the refinements is reflected in both the figures and the tabulated information. Selected bond lengths and bond angles are provided in Table 2.

The refined crystal structure of $La_3Sb_3Zn_2O_{14}$ is shown in Figure 5 and the individual coordination polyhedra are depicted in Figure 6. The rare earth ion is found in an 8-coordinated distorted cube of oxygen atoms. Antimony is octahedrally coordinated to oxygen. Zinc, conversely, takes on two different coordinations with oxygen: Zn1 is in an octahedron, while Zn2 is in a nominally 8-coordinated cavity. The initial setting of Zn2 on the 3b site (0, 0, ½), however, resulted in a large thermal parameter for this special position in all of the structure refinements (B=4-5 $Å^2$). The origin of this apparently high thermal parameter is that the Zn^{2+} ion is too small to sit in the center of this nominally 8-coordinated cavity. Therefore, the position of Zn2 was allowed to displace slightly off center in the cavity through refinements placing it at the *18g* site (*x*, 0, ½) with 1/6 site occupation (the sum of the occupancies in each cavity = 1). This resulted in stable refinements with improved thermal parameters (B~0.2-0.7 $Å^2$) for Zn2. The same structure was found for all the rare earth variants studied. There are thus four different pairs of Zn2-O separations in the 8-coordinated cavity. The four shortest separations are within the normal range expected for Zn^{2+} in tetrahedral coordination with oxygen, while the long ones are too long to represent bonding distances. Therefore, it is most appropriate to describe Zn2's coordination as being 4-fold, in a distorted tetrahedron. The coordination environment of Zn2 is depicted in Figure 6; its tetrahedron is highlighted.

As expected, the lattice parameters decrease with decreasing ionic radius of the RE^{3+}, as shown in Figure 7. The bond lengths in the 8-coordinated distorted RE-O cube range from 2.40-2.63 Å for $La_3Sb_3Zn_2O_{14}$ to 2.33-2.55 for $Gd_3Sb_3Zn_2O_{14}$. This general decrease in RE-O bond lengths along the rare earth series indicates a movement toward the formation of regular rare earth-oxygen cubes with decreasing rare earth radius. While the Sb-O bond lengths do not change their values much on going from La (1.93-2.01 Å) to Gd (1.94-1.99 Å), the O2-Sb-O2 angle changes more substantially, from 86.2° (La) to 83.3° (Gd). A similar distortion is observed for the Zn1O6 octahedra. Indeed, the Zn1-O distance in the La compound (2.14 Å) matches well with that in the Gd compound (2.12 Å). In contrast, the O3-Zn1-O3 angle varies from 80.9° in the La case to 78.5° in the Gd case. As shown in the inset of Figure 7, the distance Zn2 is displaced from its ideal site in the cube center decreases in going from La to Gd. In this manner, Zn2 moves toward the center of its nominally 8-fold cavity with decreasing ionic radius of the rare earth. The increase in O1-Zn2-O1 bond angles (157° to 165°) from La to Gd indicates a slight expansion of the polyhedra in the *c* direction, while the decrease in Zn2-O1 bond lengths are evidence of a contraction in the *ab* plane. The RE-O and Sb-O distances are overall normal as expected from the sum of the relevant ionic radii.[18]

The relationship $RE_3Sb_3Zn_2O_{14}$ shares with its parent cubic pyrochlore can be observed by considering the specific metal atom positions. Indeed, RE and Sb would be on the A and B positions in an $A_2B_2O_7$ pyrochlore structure. However, the networks of interpenetrating RE and Sb tetrahedra that would be present in the pyrochlore are absent in $RE_3Sb_3Zn_2O_{14}$ because Zn1 and Zn2 order to form $ZnRE_3$ and $ZnSb_3$ planes, respectively, on both the A and B pyrochlore sites. The ordering scheme results in the presence of two distinct 2D Kagome lattices (Figure 8), one of which is magnetic (the RE sites) and one of which is not (the Sb sites), and gives rise to the structural formula of the $RE_3Sb_3Zn_2O_{14}$ structure type as $[RE_3Zn][ZnSb_3]O_{14}$. The symmetry is reduced from cubic (*Fd-3m*) to rhombohedral (*R-3m*). The parameters of the rhombohedral unit cell (*a,c*) are related to those of the cubic pyrochlore structure ($a_{pyrochlore}$) by $a \approx \sqrt{2}a_{pyrochlore}$ and $c \approx \sqrt{3}a_{pyrochlore}$. The RE-RE separations of the Kagome planes are all equivalent and equal to (*a*/2) Å. The Kagome planes have A-B-C stacking, as dictated by the rhombohedral symmetry, resulting in interlayer RE-RE separations that are all equivalent and equal to (*c*/3) Å. The relative offset of the kagome nets is depicted in Figure 9, as well as a top-down view showing the directionality of the RE-O1 bonds.

Magnetic Susceptibility and Field Dependent Magnetization

$Pr_3Sb_3Zn_2O_{14}$

The temperature dependence of magnetic susceptibility for $Pr_3Sb_3Zn_2O_{14}$ and the reciprocal susceptibility are shown in Figure 10. Samples were fit to the Curie-Weiss law $\chi = \chi_0 + \frac{C}{T-\theta_{CW}}$ where C is the Curie Constant, θ_{CW} the Weiss temperature, and χ_0 the temperature independent contribution. The effective moments were then calculated using the relationship, $\mu_{eff} \propto 2.83\sqrt{C}$. A linear fitting of the Curie-Weiss law in the temperature range 100-300 K gives an effective moment of 3.22 μ_B /Pr and a Weiss temperature of -34.8 K; θ_{CW} is antiferromagnetic. A χ_0 of 0.000005 emu Oe^{-1} mol Pr^{-1} was used in the calculation. The μ_{eff} obtained for Pr^{3+} is a bit lower than the expected free ion value of 3.58 μ_B. While the difference between the measured and the free ion value could be attributed to the presence of Pr^{4+}, which has a free ion value of 2.54 μ_B, the structure determination of $Pr_3Sb_3Zn_2O_{14}$ does not indicate a nonstoichiometry. Moreover, a compound containing both Pr^{3+} and Pr^{4+} would be dark in color, not the very light green hue that the compound under investigation assumes. The possibility of the presence of Pr^{4+} can therefore be ruled out. Similar moments have been observed in other Pr^{3+}-containing oxides, including Pr_3IrO_7 (3.26 μ_B/Pr), $Pr_{0.01}U_{0.99}O_2$ (3.0 μ_B/Pr), and $Pr(C_2H_5SO_4)_3$*$9H_2O$ (3.3 μ_B/Pr).[19,20] It is well-known that the higher multiplets in praseodymium are located very close to the ground one. This can make the magnetic moment of Pr^{3+} more dependent on crystal field effects, often resulting in lower than expected moments for Pr^{3+}-containing compounds.[21]

The field dependent magnetization curves up to fields of H =9 T at 2 and 100 K are included as insets to Figure 10. At both high and low temperatures, the *M(H)* response is reversible and shows a linear magnetization with applied field without any signs of saturation. The broad feature in the susceptibility at around 20 K suggests the presence of some type of magnetic ordering, and has not yet been studied. The small upturn in susceptibility observed at the lowest temperatures studied is due the presence of either a magnetic impurity or uncoupled spins. Both this low T upturn and the broad peak near 20 K are reproducible in different preparations of the Pr variant.

$Nd_3Sb_3Zn_2O_{14}$

The magnetic susceptibility and inverse susceptibility of $Nd_3Sb_3Zn_2O_{14}$ are shown in Figure 11. No χ_0 was used in the calculation. The inverse susceptibility plot shows the type of behavior typical for many rare earth systems, with a gradual change in slope, implying a change in effective magnetic moment, on cooling. The inverse susceptibilities at high and low temperatures differ due to low-lying crystal field levels. Nd^{3+} has a 10-fold degenerate ground state, which is separated into five Kramer's doublets.[22] Thus, as is required to determine the properties of the magnetic ground state (the lowest energy, low temperature configuration of the 4f electrons) the magnetic data were fit to the Curie-Weiss law in the temperature range 1.8-10 K. This yielded a moment of 2.30 μ_B/Nd and a Weiss theta of -0.16 K, the latter of which is indicative of very weak antiferromagnetic interactions. Previous studies have also reported small absolute values for the Weiss temperature in Nd-based oxides, with θ_{CW} = 0.06 K in $Nd_2Zr_2O_7$, θ_{CW} = -0.069 K in $Nd_2Pb_2O_7$, and θ_{CW} = -0.31 K in $Nd_2Sn_2O_7$.[23,24] Although 2.30 μ_B/Nd is smaller than the μ_{eff} value of Nd^{3+} (3.62 μ_B) expected for the free Nd^{3+} ion in the J=9/2 Hund's rule ground state, it is similar to that observed for several neodymium pyrochlores, such as $Nd_2Ir_2O_7$ (2.30 μ_B) and $Nd_2Zr_2O_7$ (2.54 μ_B). [24,25]

The field dependent magnetizations, *M (H)*, at temperatures of T=2 and 100 K for $Nd_3Sb_3Zn_2O_{14}$ are shown as insets to Figure 11. The H-dependent magnetization (M) at 100 K is reversible and shows a linear response up to μ_0H= 9 T with no signs of saturation. The *M (H)* at 2 K, however, reveals a nonlinear variation of the magnetization as a function of applied field and the appearance of saturation at roughly 1.25 μ_B/Nd, a little more than half the value of the Curie-Weiss moment for Nd^{3+} in $Nd_3Sb_3Zn_2O_{14}$. A saturation value of roughly half the effective moment in polycrystalline samples is often characteristic of powder averaging of Ising spins, and has been observed in several neodymium pyrochlores.[26]

$Sm_3Sb_3Zn_2O_{14}$

Figure 12 shows the temperature dependence of magnetic susceptibility and inverse susceptibility in $Sm_3Sb_3Zn_2O_{14}$. As seen in many Sm compounds, the high temperature susceptibility of $Sm_3Sb_3Zn_2O_{14}$ has a large temperature-independent Van Vleck paramagnetism contribution from the first excited J=7/2 multiplet of Sm^{3+}.[27] The Curie-Weiss law was therefore fit in the low temperature range 4-13 K, yielding a θ_{CW} of -8.51 and μ_{eff} of 0.53 μ_B/Sm. No χ_0 was used in the calculation. The negative Weiss temperature denotes antiferromagnetic exchange

between spins. While the μ_{eff} value is somewhat smaller than the expected free ion value of 0.83 μ_B/Sm, it is close to the effective moment calculated for several reported samarium pyrochlores, including $Sm_2Zr_2O_7$ (0.50 μ_B/Sm).[28] An even smaller moment of 0.15 μ_B has been reported for $Sm_2Ti_2O_7$.[28] The low effective moments in these samarium compounds are likely related to the large crystal field splitting of the lowest J=5/2 multiplet.

The magnetization at various applied fields for $Sm_3Sb_3Zn_2O_{14}$ is shown in the inset to Figure 12. The *M(H)* plot at 100 K is reversible and reveals a linear response up to μ_0H= 9 T . At 2 K, however, there is an irreversible response with the appearance of a small amount of hysteresis between the field increasing and field decreasing. This hysteresis was found to be reproducible when the field was swept at different rates.

$Eu_3Sb_3Zn_2O_{14}$

Shown in Figure 13 is the temperature dependent magnetic susceptibility of $Eu_3Sb_3Zn_2O_{14}$ from 1.8 to 300 K. The magnetic susceptibility for Eu^{3+} compounds typically increases with decrease in temperature, attains a temperature-independent constant value at high T (characteristic of Van Vleck paramagnetism), and then increases rapidly around 0-10 K.[1,29] This is observed for $Eu_3Sb_3Zn_2O_{14}$. The resulting χ_0 is 0.0011 emu Oe^{-1} mol Eu^{-1}. In the range 200-300 K, an effective moment of 3.52 μ_B/Eu and θ_{CW} of -114.7 K were obtained. The magnitude and sign of the Weiss temperature are indicative of strong antiferromagnetic interactions between europium spins. There is a correlation between the interaction strength observed from the Curie-Weiss fit and the point at which there appears to be the onset of temperature independent paramagnetism. Additional work, such as heat capacity or neutron diffraction measurements, is necessary to explore whether magnetic ordering is present in this compound. The effective moment calculated for europium through the Curie-Weiss fit corresponds well with the expected free-ion value of 3.58 μ_B/ Eu^{3+}. The slight upturn observed in the magnetic susceptibility at low temperatures may be due to the presence of a magnetic impurity; this has been observed in other Eu^{3+} oxides, such as Eu_3MoO_7 and $Eu_2Ti_2O_7$.[29,30] The field-dependent magnetization plots at 2 and 100 K provided in the inset to Figure 13 for $Eu_3Sb_3Zn_2O_{14}$ are both linear and reversible with the field increasing and decreasing.

$Gd_3Sb_3Zn_2O_{14}$

The temperature dependence of magnetic susceptibility of $Gd_3Sb_3Zn_2O_{14}$ is shown in Figure 14. This is the most straightforward of the behaviors observed. $\chi(T)$ was fit to the Curie-Weiss law from 150 to 300 K. No χ_0 was used in the calculation. An effective magnetic moment of 7.83 μ_B/Gd was obtained from the Curie-Weiss fit, which is close to the expected value of 7.94 μ_B/Gd for the free ion $^8S_{7/2}$ ground state of Gd^{3+}. A Weiss temperature of -2.32 K was extrapolated from the high temperature fit, which indicates the presence of antiferromagnetic interactions between Gd^{3+} spins. The H-dependent magnetization (M) plots of $Gd_3Sb_3Zn_2O_{14}$ at 2 and 100 K are presented as insets to the susceptibility graph in Figure 14. The *M(H)* plot at 100 K is both reversible and linear up to an applied field of μ_0H= 9 T . Conversely, the *M(H)* plot at 2 K reveals a nonlinear relationship between magnetization and the applied field and saturation at about 7.21 μ_B/Gd, a little less than the value of the calculated Curie-Weiss effective moment and representative of the alignment of all the Gd spins in the powder sample along the applied field direction by a field of roughly μ_0H= 8 T.

Conclusion

The structure of $RE_3Sb_3Zn_2O_{14}$ (RE=La, Pr, Nd, Sm, Eu, Gd) was solved using synchrotron x-ray diffraction. It is fully layered and crystallizes in a rhombohedral space group derived from the pyrochlore. The ordering of the atoms are Zn:RE in the A sites and Zn:Sb in the B sites with the ratio 1:3. The distribution of the RE, Sb, and Zn cations in $RE_3Sb_3Zn_2O_{14}$ allows for two distinctive 2D Kagome lattices composed of Sb^{5+} and RE^{3+} within the rhombohedral pyrochlore structure. The structure has an ordered distribution of cations in the magnetic rare earth kagome lattice, with slight disorder in the nonmagnetic lattice from the disordered displacement of one of the zinc atoms from its polyhedron center. If this off center Zn displacement has any influence on the rare earth magnetism at all, it should be extremely weak. Further experimental characterization will be required to clarify this aspect of the magnetic properties of compounds in this family. Magnetic susceptibility measurements on $RE_3Sb_3Zn_2O_{14}$ (RE=Pr, Nd, Sm, Eu, Gd) indicate that these compounds display antiferromagnetic interactions. No magnetic ordering is observed above 1.8 K for this series of compounds, however, with the possible exception of the Pr and Eu cases. It should be noted that 2D rare earth Kagome lattices are very rare; to our knowledge, this is the first series of compounds to be reported containing idealized 2D rare earth Kagome lattices with no other magnetic ions present. The known

examples of ordered rhombohedral pyrochlores of this type are extremely limited, possibly due to the required ion size ratios, but also possibly due to what sometimes seems to be the unique character of Sb^{5+} in oxides. Further characterization of these new materials, especially the magnetic properties of single crystals, and the possible ordered magnetic structures for the different variants at lower temperatures, would be of significant interest.

Acknowledgements

All the research at Princeton was supported by the U.S. Department of Energy, Division of Basic Energy Sciences, Grant No. DE-FG02-08ER46544. We thank the beamline scientists at 11-BM at the Advanced Photon Source (APS) for quickly providing the high quality diffraction data employed. Use of the Advanced Photon Source at Argonne National Laboratory was supported by the U. S. Department of Energy, Office of Science, Office of Basic Energy Sciences, under Contract No. DE-AC02-06CH11357.

References

1 B. Vijaya Kumar, R. Velchuri, V. Rama Devi, B. Sreedhar, G. Prasad, D. Jaya Prakash, M. Kanagaraj, S. Arumugam and M. Vithal, *J. Solid State Chem.*, 2011, **184**, 264–272.
2 J. Lian, L. M. Wang, S. X. Wang, J. Chen, L. A. Boatner and R. C. Ewing, *Phys. Rev. Lett.*, 2001, **87**, 145901.
3 T. Yamamoto, R. Kanno, Y. Takeda, O. Yamamoto, Y. Kawamoto and M. Takano, *J. Solid State Chem.*, 1994, **109**, 372–383.
4 B. C. den Hertog and M. J. P. Gingras, *Phys. Rev. Lett.*, 2000, **84**, 3430–3433.
5 H. J. Silverstein, K. Fritsch, F. Flicker, A. M. Hallas, J. S. Gardner, Y. Qiu, G. Ehlers, A. T. Savici, Z. Yamani, K. A. Ross, B. D. Gaulin, M. J. P. Gingras, J. A. M. Paddison, K. Foyevtsova, R. Valenti, F. Hawthorne, C. R. Wiebe and H. D. Zhou, *Phys. Rev. B*, 2014, **89**, 054433.
6 M. Hanawa, J. Yamaura, Y. Muraoka, F. Sakai and Z. Hiroi, *J. Phys. Chem. Solids*, 2002, **63**, 1027–1030.
7 J. S. Gardner, M. J. P. Gingras and J. E. Greedan, *Rev. Mod. Phys.*, 2010, **82**, 53–107.
8 J. L. Atwood, *Nat. Mater.*, 2002, **1**, 91–92.
9 I. E. Grey, W. G. Mumme, T. J. Ness, R. S. Roth and K. L. Smith, *J. Solid State Chem.*, 2003, **174**, 285–295.
10 M. P. Shores, E. A. Nytko, B. M. Bartlett and D. G. Nocera, *J. Am. Chem. Soc.*, 2005, **127**, 13462–13463.
11 J. S. Helton, K. Matan, M. P. Shores, E. A. Nytko, B. M. Bartlett, Y. Yoshida, Y. Takano, A. Suslov, Y. Qiu, J.-H. Chung, D. G. Nocera and Y. S. Lee, *Phys. Rev. Lett.*, 2007, **98**, 107204.
12 F. Bert, A. Olariu, A. Zorko, P. Mendels, J. C. Trombe, F. Duc, M. A. de Vries, A. Harrison, A. D. Hillier, J. Lord, A Amato and C. Baines, *J. Phys. Conf. Ser.*, 2009, **145**, 012004.
13 D. V. Pilon, C. H. Lui, T.-H. Han, D. Shrekenhamer, A. J. Frenzel, W. J. Padilla, Y. S. Lee and N. Gedik, *Phys. Rev. Lett.*, 2013, **111**, 127401.

14 P. Bordet, I. Gelard, K. Marty, A. Ibanez, J. Robert, V. Simonet, B. Canals, R. Ballou and P. Lejay, *J. Phys. Condens. Matter*, 2006, **18**, 5147.
15 S. Ghosh, S. Datta, H. Zhou, M. Hoch, C. Wiebe and S. Hill, *J. Appl. Phys.*, 2011, **109**, 07E137.
16 W. T. Fu and D. J. W. IJdo, *J. Solid State Chem.*, 2014, **213**, 165–168.
17 K. Li, Y. Hu, Y. Wang, T. Kamiyama, B. Wang, Z. Li and J. Lin, *J. Solid State Chem.*, 2014, **217**, 80–86.
18 R. D. Shannon, *Acta Crystallogr. Sect. A*, 1976, **32**, 751–767.
19 H. Nishimine, M. Wakeshima and Y. Hinatsu, *J. Solid State Chem.*, 2004, **177**, 739–744.
20 J. F. Vente, R. B. Helmholdt and D. J. W. IJdo, *J. Solid State Chem.*, 1994, **108**, 18–23.
21 S. Turczynski, K. Orlinski, D. A. Pawlak, R. Diduszko, J. Mucha, M. Pekala, J. F. Fagnard, P. Vanderbemden and M. A. Carpenter, *Cryst. Growth Des.*, 2011, **11**, 1091–1097.
22 R. L. Carlin, *Magnetochemistry*, Springer Science & Business Media, 2012.
23 A. M. Hallas, A. M. Arevalo-Lopez, A. Z. Sharma, T. Munsie, J. P. Attfield, C. R. Wiebe and G. M. Luke, *Phys. Rev. B*, 2015, **91**, 104417.
24 M. C. Hatnean, M. R. Lees, O. A. Petrenko, D. S. Keeble, G. Balakrishnan, M. J. Gutmann, V. V. Klekovkina and B. Z. Malkin, *Phys. Rev. B*, 2015, **91**, 174416.
25 H. Nishimine, M. Wakeshima and Y. Hinatsu, *J. Solid State Chem.*, 2004, **177**, 739–744.
26 A. M. Hallas, A. M. Arevalo-Lopez, A. Z. Sharma, T. Munsie, J. P. Attfield, C. R. Wiebe and G. M. Luke, *Phys. Rev. B*, 2015, **91**, 104417.
27 S. K. Malik and R. Vijayaraghavan, *Pramana*, 1974, **3**, 122–132.
28 S. Singh, S. Saha, S. K. Dhar, R. Suryanarayanan, A. K. Sood and A. Revcolevschi, *Phys. Rev. B*, 2008, **77**, 054408.
29 H. Nishimine, M. Wakeshima and Y. Hinatsu, *J. Solid State Chem.*, 2005, **178**, 1221–1229.
30 P. Dasgupta, Y. M. Jana, A. Nag Chattopadhyay, R. Higashinaka, Y. Maeno and D. Ghosh, *J. Phys. Chem. Solids*, 2007, **68**, 347–354.

Tables

Table 1: Refinement Summary of $RE_3Sb_3Zn_2O_{14}$ @ 295 K

	La	Pr	Nd	Sm	Eu	Gd
RE ***(9e)***	(½,0,0)	(½,0,0)	(½,0,0)	(½,0,0)	(½,0,0)	(½,0,0)
B (Å^2)	0.44(7)	0.37(4)	0.30(3)	0.29(4)	0.27(6)	0.28(1)
Zn1 ***(3a)***	(0,0,0)	(0,0,0)	(0,0,0)	(0,0,0)	(0,0,0)	(0,0,0)
B (Å^2)	0.35(9)	0.31(6)	0.32(6)	0.22(6)	0.25(4)	0.22(1)
Zn2 (*18g*)	(0.0525(3),0,½)	(0.0457(2),0,½)	(0.0425(2),0,½)	(0.0400(2),0,½)	(0.0372(2),0,½)	(0.0335(3),0,½)
B (Å^2)	0.70(1)	0.60(1)	0.61(1)	0.59(9)	0.62(3)	0.21(2)
Sb ***(9d)***	(1/2,0,1/2)	(1/2,0,1/2)	(1/2,0,1/2)	(1/2,0,1/2)	(1/2,0,1/2)	(1/2,0,1/2)
B (Å^2)	0.53(1)	0.50(9)	0.49(6)	0.41(1)	0.44(9)	0.41(1)
O1 ***(6c)***	(0,0,z)	(0,0,z)	(0,0,z)	(0,0,z)	(0,0,z)	(0,0,z)
z	0.3903(3)	0.3883(3)	0.3883(2)	0.3873(3)	0.3868(3)	0.3873(4)
B (Å^2)	0.39(8)	0.30(1)	0.21(2)	0.39(6)	0.21(8)	0.49(8)
O2 (18h)	(x,x̄,z)	(x,x̄,z)	(x,x̄,z)	(x,x̄,z)	(x,x̄,z)	(x,x̄,z)
x	0.5370(2)	0.5358(2)	0.5358(6)	0.5352(3)	0.5344(6)	0.5325(3)
z	0.1471(9)	0.1467(7)	0.1465(4)	0.1462(6)	0.1462(2)	0.1459(2)
B (Å^2)	0.27(4)	0.35(6)	0.45(7)	0.30(2)	0.28(9)	0.46(5)
O3 (18h)	(x,x̄,z)	(x,x̄,z)	(x,x̄,z)	(x,x̄,z)	(x,x̄,z)	(x,x̄,z)
x	0.1439(2)	0.1448(5)	0.1453(9)	0.1466(1)	0.1470(1)	0.1477(3)
z	-0.0581(7)	-0.0568(9)	-0.0564(8)	-0.0559(1)	-0.0555(9)	-0.0550(2)
B (Å^2)	0.27(1)	0.31(1)	0.24(9)	0.26(4)	0.21(1)	0.40(1)
a **(Å)**	7.54083(1)	7.48239(4)	7.46517(1)	7.42707(3)	7.41302(7)	7.40283(7)
c **(Å)**	17.56160(2)	17.43821(9)	17.38259(5)	17.29581(6)	17.25317(1)	17.21335(1)
R_{wp} (%)	11.83	9.46	9.11	10.44	9.95	11.6
R_p **(%)**	9.69	7.53	7.17	8.38	7.86	8.54
χ^2	4.09	3.75	3.41	3.70	3.95	4.34

Table 2: Selected bond distanced (Å) and bond angles (°) for $RE_3Sb_3Zn_2O_{14}$ (RE = La, Pr, Nd, Sm, Eu, Gd @ 295K)

RE	La	Pr	Nd	Sm	Eu	Gd
REO_8 polyhedron						
RE-O1	2.396(3) x2	2.363(3) ×2	2.357(3) ×2	2.338(3) ×2	2.330(3) ×2	2.330(3) ×2
RE-O2	2.630(4) x2	2.601(3) ×2	2.589(3) ×2	2.570(3) ×2	2.561(3) ×2	2.546(4) ×2
RE-O3	2.553(7) x2	2.518(6) ×2	2.505 (4) ×2	2.480(3) ×2	2.471(1) ×2	2.459(2) ×2
	2.553(1) x2	2.518(1) ×2	2.505(9) ×2	2.480(9) ×2	2.470(5) ×2	2.458(2) ×2
Average RE-O	2.533(1)	2.500(2)	2.489(4)	2.467(5)	2.458(3)	2.448(2)
Intraplane RE-RE	3.770(4)	3.741(2)	3.732(6)	3.713(5)	3.706(5)	3.701(4)
Interplane RE-RE	5.853(9)	5.812(7)	5.794(2)	5.765(3)	5.751(1)	5.737(8)
SbO_6 octahedron						
Sb-O2	2.00(9)×4	2.00(1) ×4	1.99(6) ×4	1.98(9) ×4	1.98(8) ×4	1.99(5) ×4
Sb-O3	1.929(3)×2	1.935(3)×2	1.935(3) ×2	1.933(3) ×2	1.933(3) ×2	1.937(4) ×2
Average Sb-O	1.98(2)	1.97(8)	1.97(5)	1.97(0)	1.96(9)	1.97(5)
O2-Sb-O3	86.2(3) ×4	85.6(7) ×4	85.4(1) ×4	84.9(3) ×4	84.7(8) ×4	84.4(1) ×4
	93.7(7) ×4	94.3(3) ×4	94.5(9) ×4	95.0(7) ×4	95.2(2) ×4	95.5(7) ×4
O2-Sb-O2	93.8(1) ×2	94.5(6) ×2	94.4(9) ×2	94.8(7) ×2	95.4(1) ×2	96.7(1) ×2
	86.2(1) ×2	85.4(4) ×2	85.5(2) ×2	85.1(3) ×2	84.6(1) ×2	83.3(1) ×2
$Zn1O_6$ octahedron						
Zn1-O3	2.13(9) ×6	2.12(3) ×6	2.12(1) ×6	2.11(9) ×6	2.11(7) ×6	2.11(7) ×6
O3-Zn1-O3	99.0(8)×6	99.9(3) ×6	100.2(9) ×6	100.8(1) ×6	101.0(7) ×6	101.5(2) ×6
	80.9(2)×6	80.0(7) ×6	79.7(3) ×6	79.1(9) ×6	78.9(3) ×6	78.4(8) ×6
$Zn2O_8$ polyhedron						
Zn2-O1	1.96(7) × 2	1.97(9) ×2	1.96(7) ×2	1.97(3) ×2	1.97(3) ×2	1.95(7) ×2
Short Zn2-O2	2.35(1)×2	2.35(9) ×2	2.37(4) ×2	2.37(1) ×2	2.37(3) ×2	2.36(9) ×2
Short Average	2.15(9)	2.16(9)	2.17(1)	2.17(2)	2.17(3)	2.16(3)
Long Zn2-O2	2.71(1)×2	2.66(8)×2	2.66(1) ×2	2.63(7) ×2	2.62(1) ×2	2.59(1) ×2
	3.02(8)×2	2.94(5) ×2	2.91(8) ×2	2.87(9) ×2	2.84(5) ×2	2.79(4) ×2
Long Average	2.86(9)	2.80(7)	2.78(9)	2.75(8)	2.73(3)	2.69(3)
O1-Zn2-O1	156.7(7)	160.0(9)	161.4(4)	162.6(7)	163.9(3)	165.4(4)

Figure Captions

Figure 1

Ball and stick figure portraying the connectivity of A (cyan) and B (pink) networks of tetrahedra that compose the $A_2B_2O_7$ pyrochlore structure. The right panel portrays the $[A_3A'][B_3B']O_{14}$ Kagome structure of the current materials, where now the substitution of A' (purple) and B' (green) cations enables the formation of discrete Kagome planes in the former (111) planes of the pyrochlore. This results in rhombohedral rather than cubic symmetry for $[A_3A'][B_3B']O_{14}$. Oxygens are omitted in both structures for clarity.

Figure 2

Rietveld refinement of $La_3Sb_3Zn_2O_{14}$ (upper panel) and $Pr_3Sb_3Zn_2O_{14}$ (lower panel) at room temperature using synchrotron x-ray diffraction data. The experimental pattern is in red, the calculated pattern in black, and the difference plot in blue. The green marks indicate Bragg reflections.

Figure 3

Rietveld refinement of $Nd_3Sb_3Zn_2O_{14}$ (upper panel) and $Sm_3Sb_3Zn_2O_{14}$ (lower panel) at room temperature using synchrotron x-ray diffraction data. The experimental pattern is in red, the calculated pattern in black, and the difference plot in blue. The green marks indicate Bragg reflections.

Figure 4

Rietveld refinement of $Eu_3Sb_3Zn_2O_{14}$ (upper panel) and $Gd_3Sb_3Zn_2O_{14}$ (lower panel) at room temperature using synchrotron x-ray diffraction data. The experimental pattern is in red, the calculated pattern in black, and the difference plot in blue. The green marks indicate Bragg reflections.

Figure 5

The crystal structure of $La_3Sb_3Zn_2O_{14}$. The magenta polyhedra represent LaO_8, the yellow polyhedra SbO_6, and the two green polyhedra $Zn1O_6$ and $Zn2O_8$, respectively.

Figure 6

The coordination polyhedra of $La_3Sb_3Zn_2O_{14}$: La (upper left), Sb (upper right), Zn1 (lower left), and Zn2 (lower right). The black zinc atom and its four black bonds portray the tetrahedron for Zn2. The different types of oxygen atoms are represented in different shades of blue. The M-O distances to the oxygen ion types are equal, e.g. Zn2 has two bonds of 1.97 Å to the light blue oxygens (O1) and two bonds of 2.35 Å to the nearest dark blue oxygens (O2).

Figure 7

The *a* and *c* lattice parameters for $RE_3Sb_3Zn_2O_{14}$ as a function of rare earth ionic radius. The pink and black points represent the *a* and *c* parameters, respectively. The standard deviations are smaller than the plotted points and so error bars are excluded from the figure. In the inset is a plot showing the distance Zn2 is displaced from its ideal position in the center of the nominally 8-fold cavity as a function of rare earth ionic radius. The error bars were obtained from the standard deviations in the refined x positions of Zn2's *18g* additional free parameter, which were propagated in the calculation of the distances.

Figure 8

Schematic of $RE_3Sb_3Zn_2O_{14}$ displaying the positions of the metal ions in the unit cell. To the right of the schematic are extended lattices showing the discrete rare earth and antimony Kagome planes in the structure.

Figure 9

On the left is a top-down view of how the Kagome nets are offset relative to one another by ABC stacking. On the right is an image portraying the directionality of the RE-O1 bonds. The oxygens positioned above the kagome plane are dark blue, while the oxygens located below the plane are light blue.

Figure 10

The DC magnetic susceptibility and inverse susceptibility of $Pr_3Sb_3Zn_2O_{14}$ measured in an applied field of 5000 Oe. The Curie-Weiss fit is shown in Cyan. The insets to the right of the MT plot show the magnetization as a function of applied field *M(H)* at 2 K (upper panel) and 100 K (lower panel).

Figure 11

Temperature-dependent magnetic susceptibility of $Nd_3Sb_3Zn_2O_{14}$ measured in an applied field of 5000 Oe. The low temperature Curie-Weiss fit is shown in black. The insets to the right of the magnetic susceptibility plot display the field-dependent magnetizations at 2K and 100 K.

Figure 12

The DC magnetic susceptibility and reciprocal susceptibility of $Sm_3Sb_3Zn_2O_{14}$ measured in an applied field of 5000 Oe. The Curie-Weiss fit is shown in red. The plots in the upper and lower panels to the right of the MT graph show the field-dependent magnetizations at 2 and 100 K, respectively.

Figure 13

Temperature-dependent magnetic susceptibility of $Eu_3Sb_3Zn_2O_{14}$ measured in an applied field of 5000 Oe. The Curie-Weiss fit is shown in red. The insets display *M(H)* plots of the compound at temperatures of 2 K (upper panel) and 100 K (lower panel).

Figure 14

Magnetic susceptibility and inverse susceptibility of $Gd_3Sb_3Zn_2O_{14}$ measured in an applied field of 5000 Oe. The Curie-Weiss fit is shown in black. The panels to the right of the susceptibility plot show the field-dependent magnetizations at temperatures of 2 and 100 K.

Figures

Figure 1

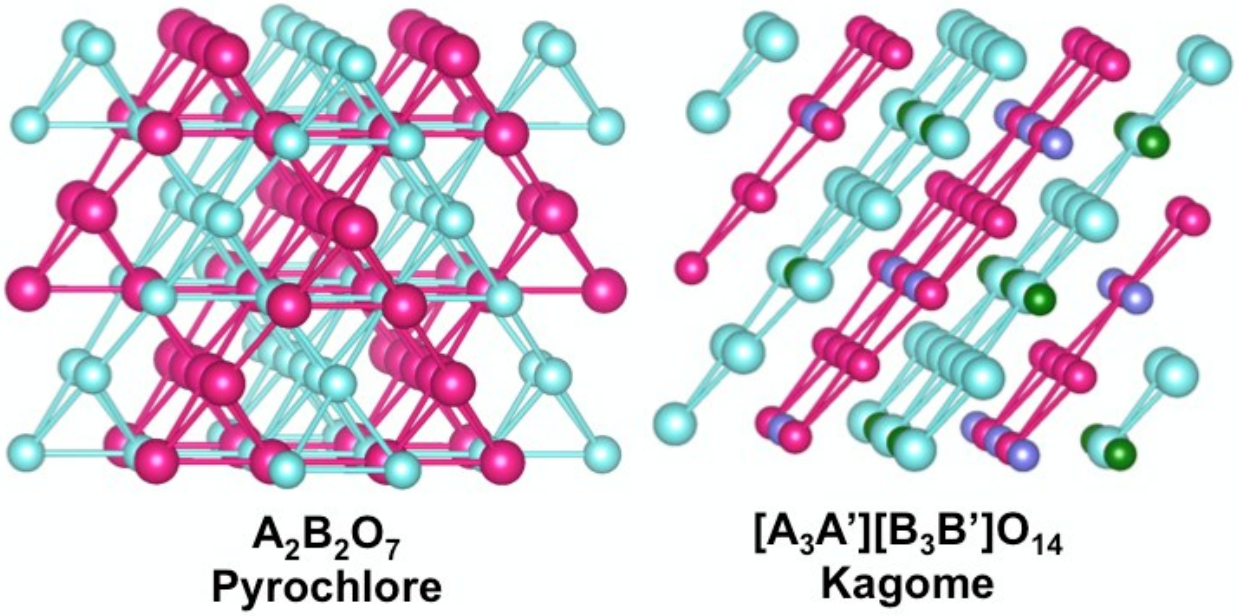

Figure 2

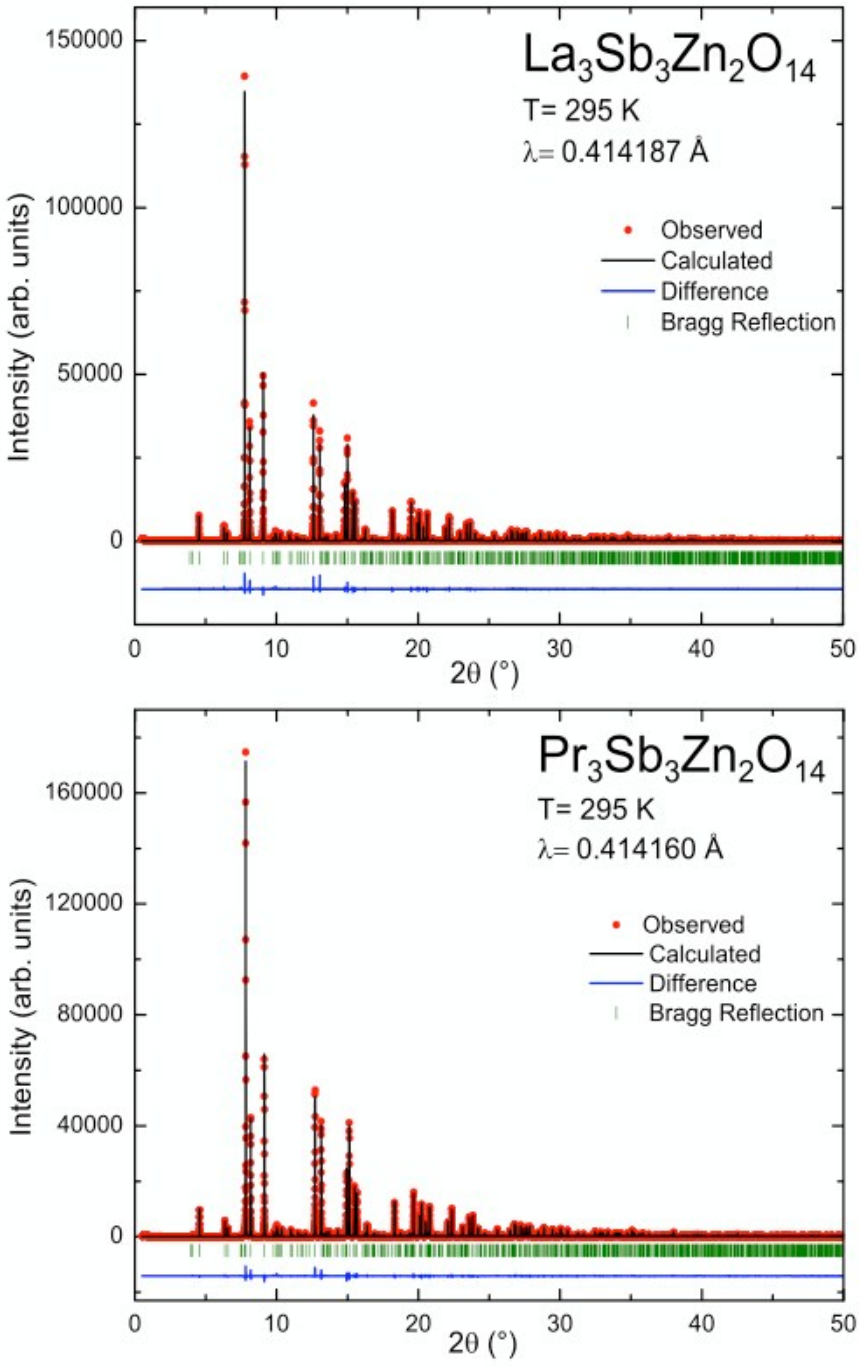

Figure 3

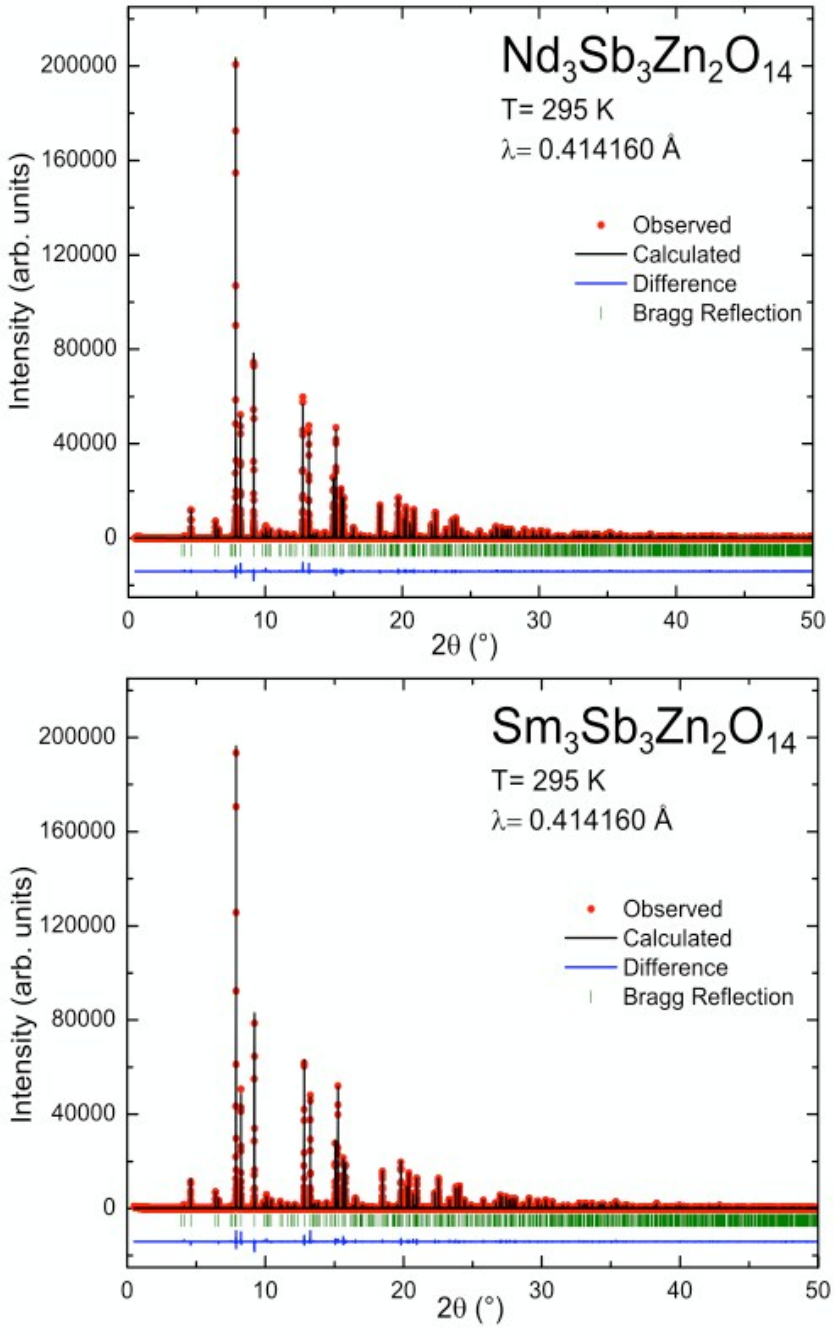

Figure 4

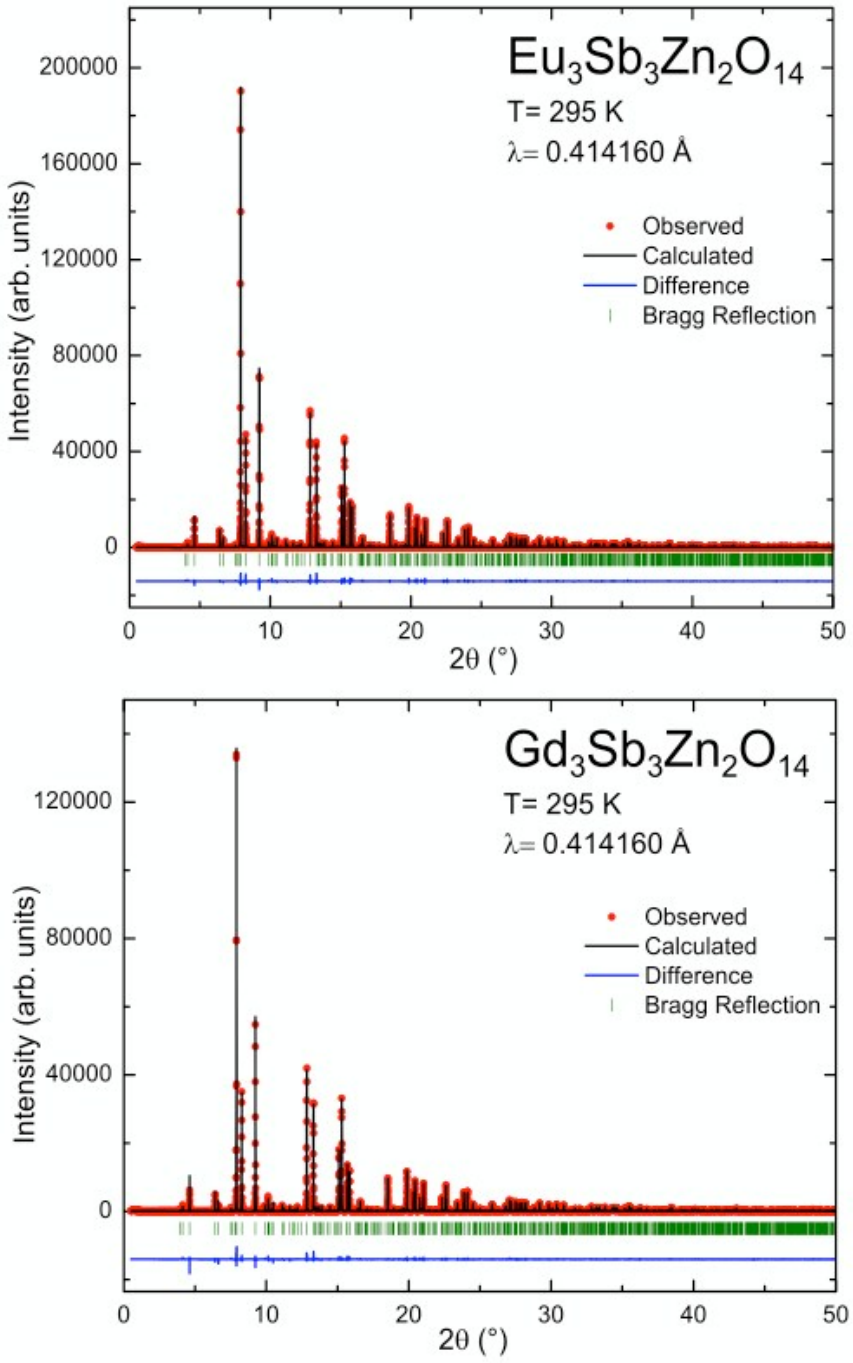

Figure 5

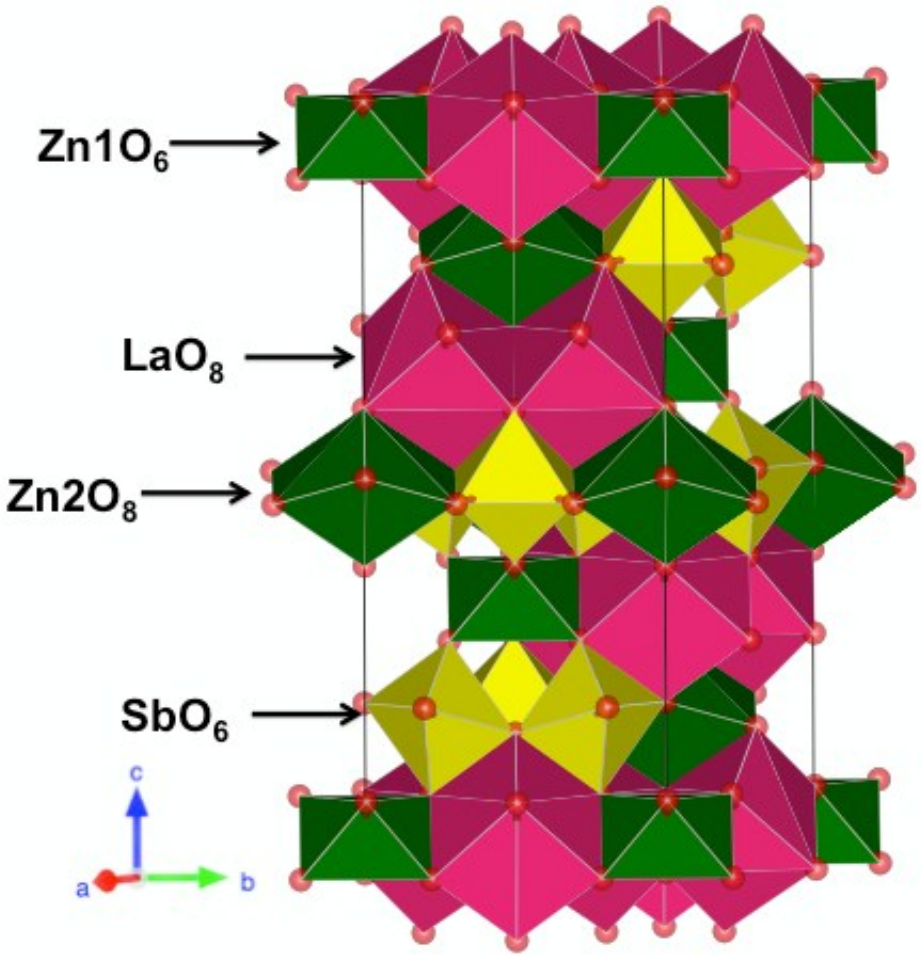

Figure 6

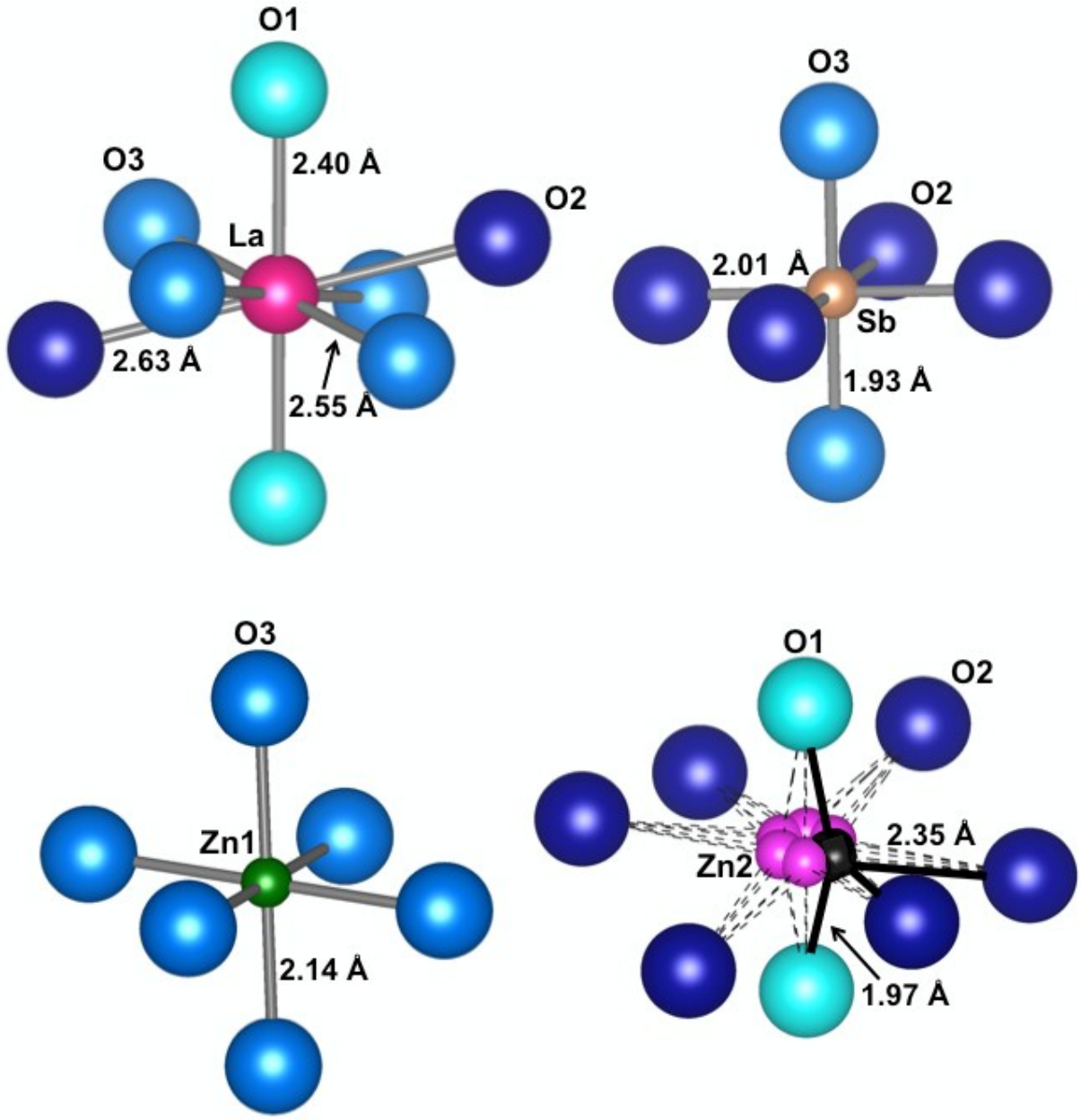

Figure 7

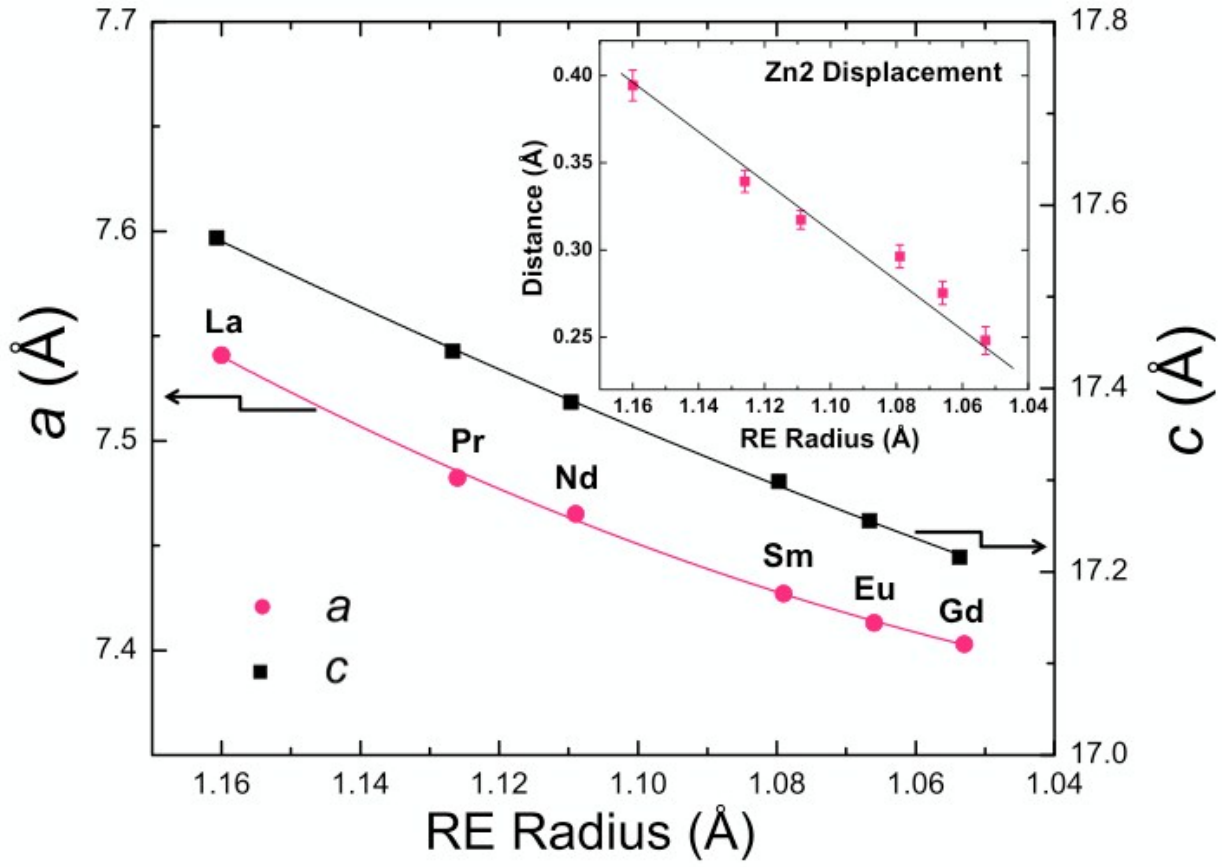

Figure 8

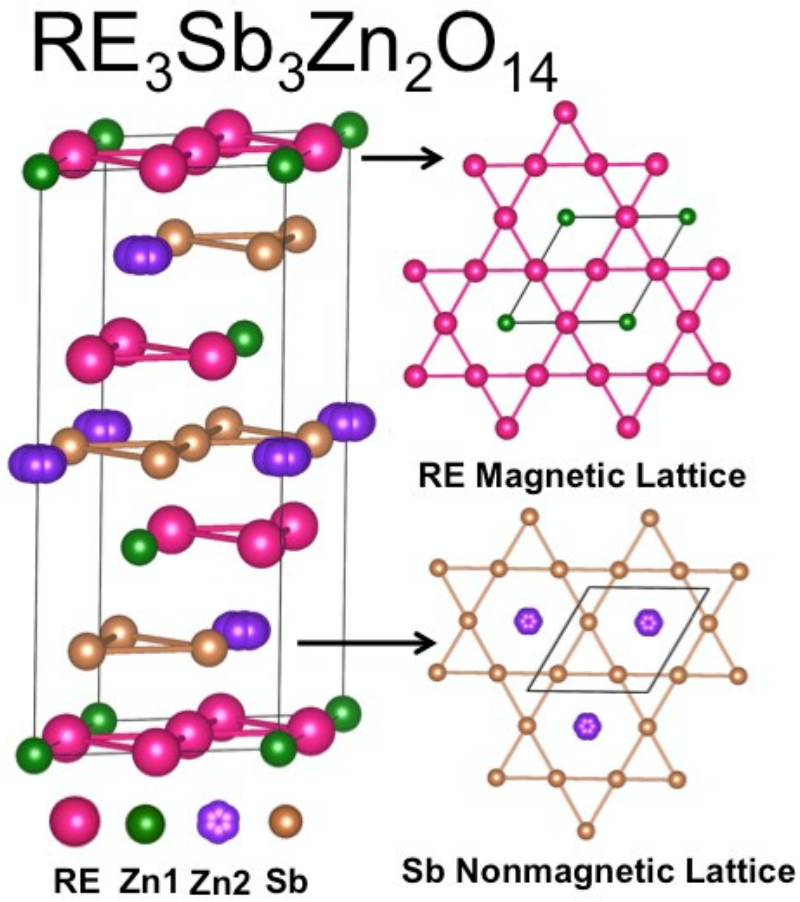

Figure 9

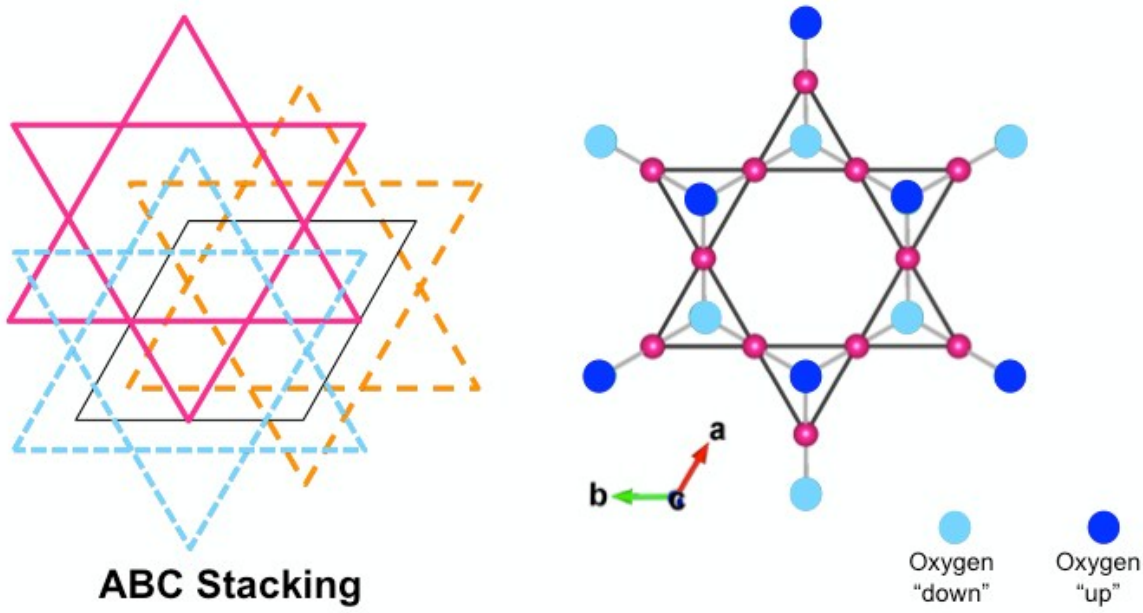

Figure 10

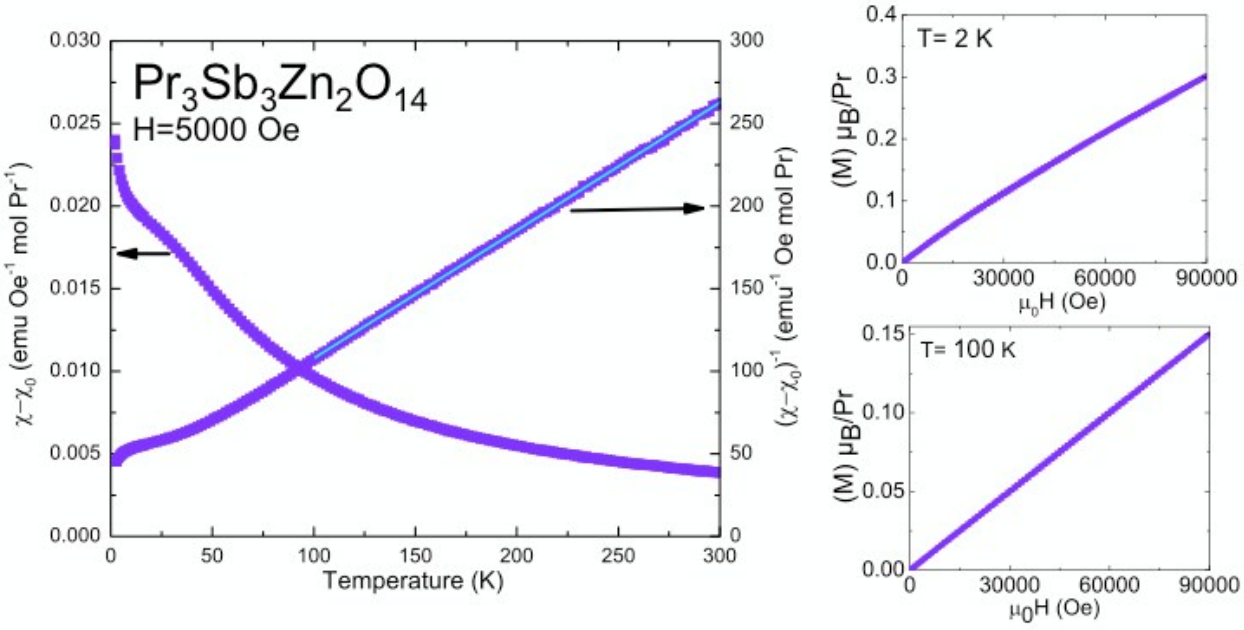

Figure 11

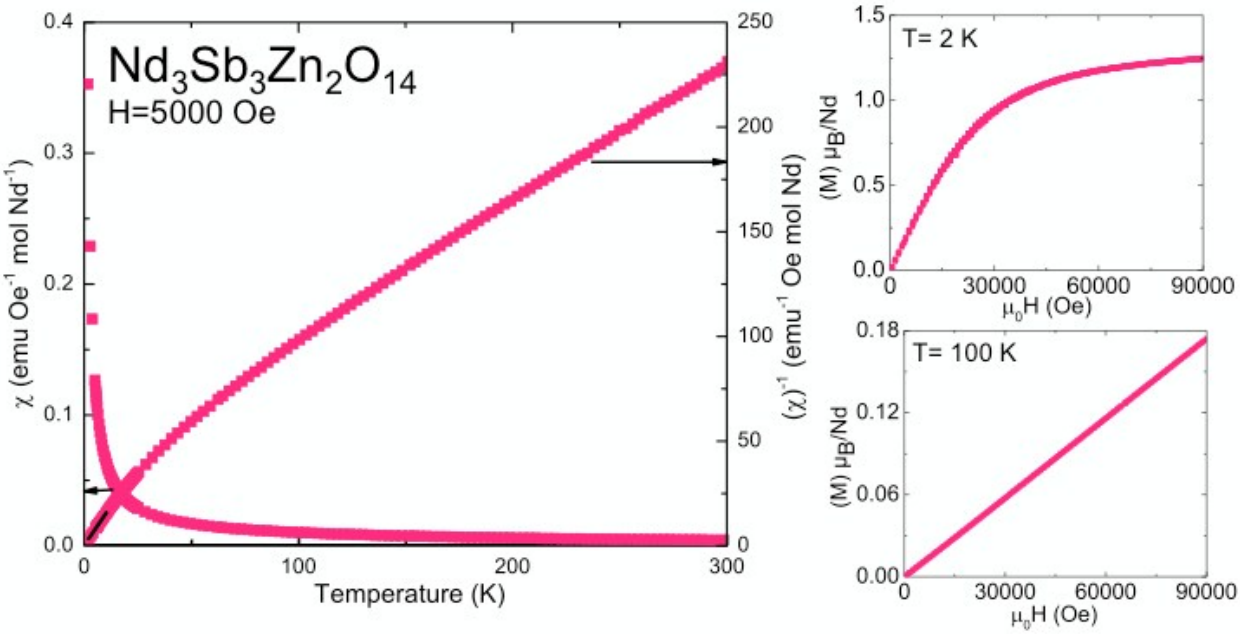

Figure 12

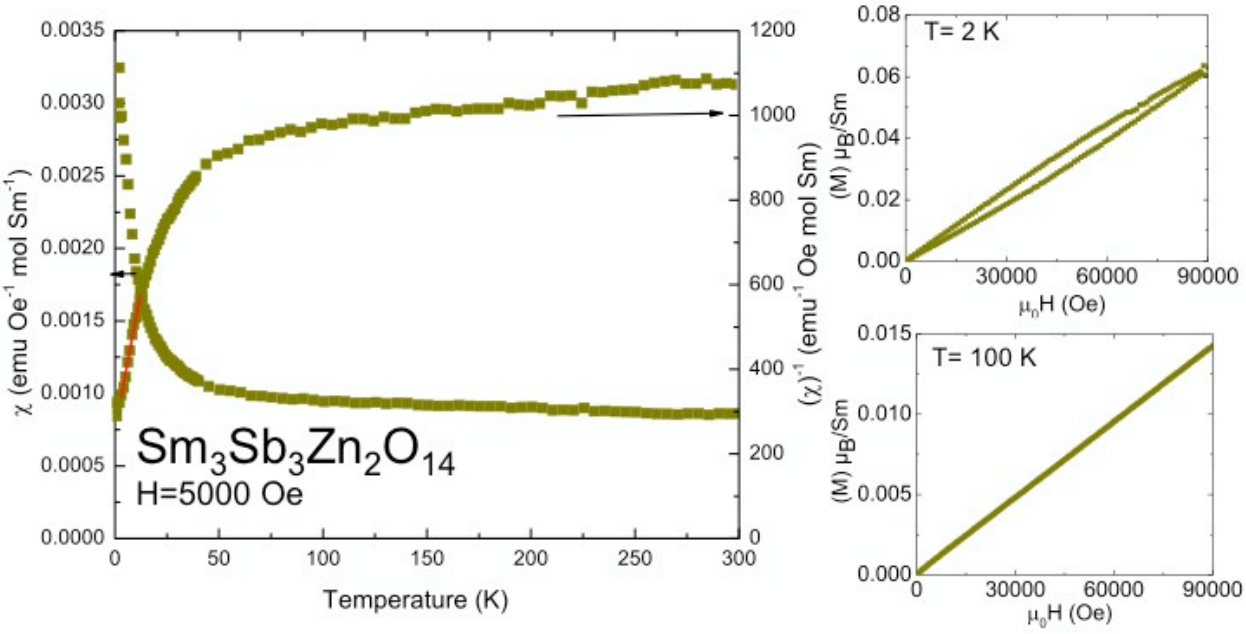

Figure 13

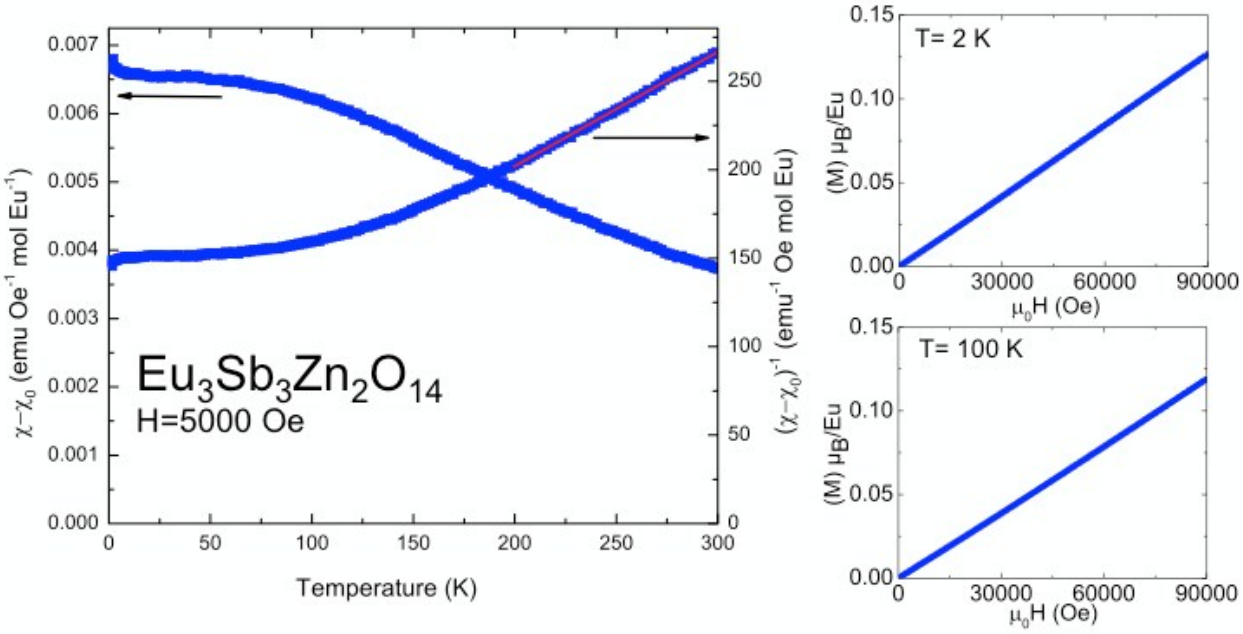

Figure 14

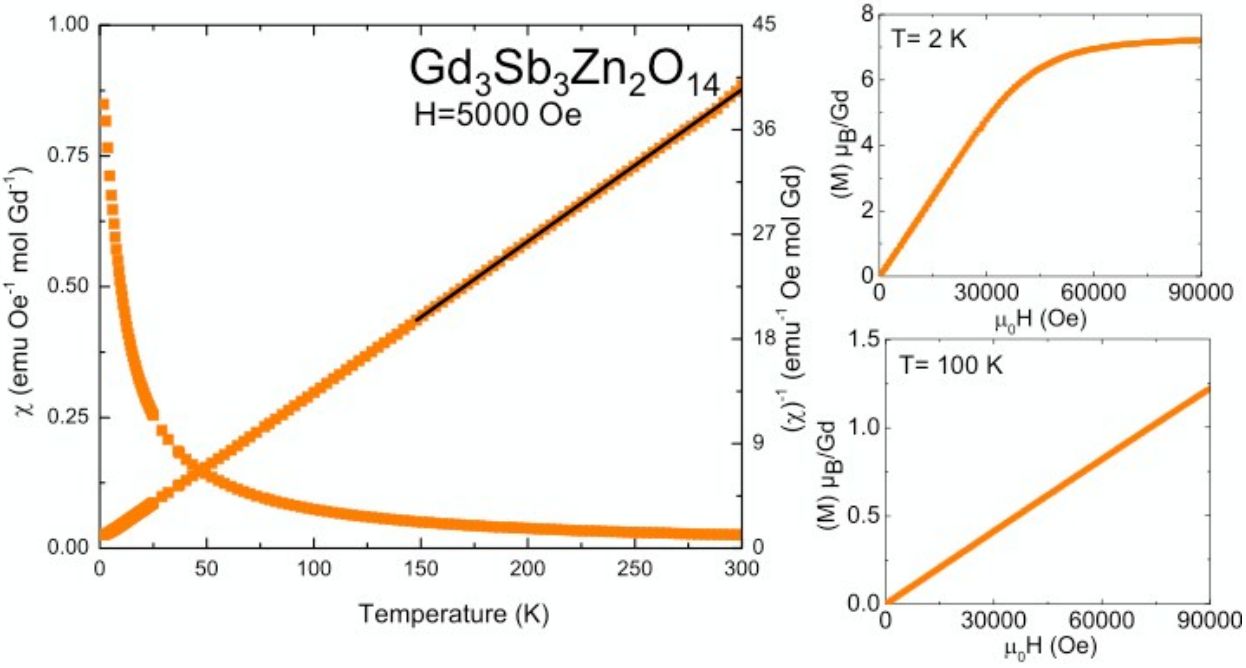

$RE_3Sb_3Zn_2O_{14}$ (RE=La, Pr, Nd, Sm, Eu, Gd): A new family of pyrochlore derivatives with rare earth ions on a 2D Kagome lattice

M.B. Sanders, J.W. Krizan, and R.J. Cava

Department of Chemistry, Princeton University, Princeton, New Jersey 08544

$RE_3Sb_3Zn_2O_{14}$ (RE=La, Pr, Nd, Sm, Eu, Gd) is a series of novel pyrochlore-related materials with 2D Kagome lattices formed by RE^{3+} and Sb^{5+}. The rare earth is the only magnetic ion in the structure; this family is therefore an archetype for exploring magnetic frustration on a 2D Kagome lattice.